PCCP

Accepted Manuscript

This is an *Accepted Manuscript*, which has been through the Royal Society of Chemistry peer review process and has been accepted for publication.

Accepted Manuscripts are published online shortly after acceptance, before technical editing, formatting and proof reading. Using this free service, authors can make their results available to the community, in citable form, before we publish the edited article. We will replace this *Accepted Manuscript* with the edited and formatted *Advance Article* as soon as it is available.

You can find more information about *Accepted Manuscripts* in the Information for Authors.

Please note that technical editing may introduce minor changes to the text and/or graphics, which may alter content. The journal's standard Terms & Conditions and the Ethical guidelines still apply. In no event shall the Royal Society of Chemistry be held responsible for any errors or omissions in this *Accepted Manuscript* or any consequences arising from the use of any information it contains.

ROYAL SOCIETY OF CHEMISTRY

www.rsc.org/pccp

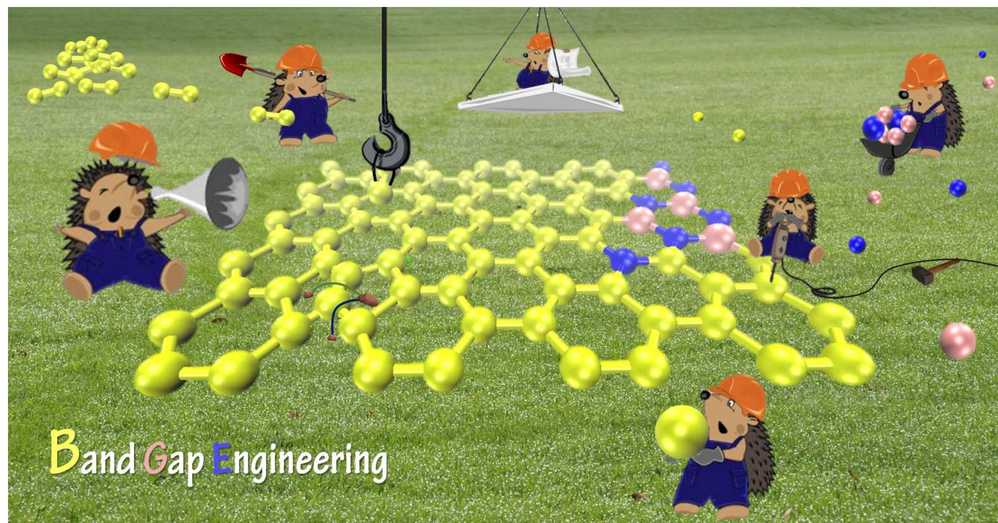

960x497mm (72 x 72 DPI)

Physical Chemistry Chemical Physics Accepted Manuscript

Line Defects and Induced Doping Effects in Graphene, Hexagonal Boron Nitride and Hybrid BNC

Narjes Ansari,[1] Fariba Nazari,[1,2] Francesc Illas[3]

[1]*Department of Chemistry, Institute for Advanced Studies in Basic Sciences, Zanjan 45137-66731, Iran*

[2]*Center of Climate Change and Global Warming, Institute for Advanced Studies in Basic Sciences, Zanjan 45137-66731, Iran*

[3]*Departament de Química Física & Institut de Química Teòrica i Computacional (IQTCUB), Universitat de Barcelona, C/Martí i Franquès 1, 08028 Barcelona, Spain*

Abstract

Effects on atomic structure and electronic properties of two dimensional graphene (G) and *h*-BN sheets related to the coexistence of dopants and defects are investigated by using density functional theory based methods. Two types of extended line defects are considered for pristine G and *h*-BN sheets. In these sheets, the presence of individual doping increases the charge transport character. Coexistence of dopants and defects tunes the band gap towards lower values and cause the direct-indirect band gap change. The relative stability and the electronic properties of various $B_xN_yC_z$ systems are analyzed in detail. We find that the structural properties of these type systems strongly depend on the orientation of grain boundaries and whether these are parallel or perpendicular to the extended line defects. The electronic structure analyses the different systems evidences the existence of absorption shifts to the visible region.

Physical Chemistry Chemical Physics Accepted Manuscript

Introduction

Newly discovered low dimensional materials (LDMs) are transforming technology in a variety of different fields going all the way from life sciences to energy and to advanced materials. LDMs have one or more physical dimension(s) constrained to the nanometer scale. This constraint implies electron confinement, a property that imparts LDMs new and unusual properties as well as new opportunities for novel engineering applications.[1] Examples of LDMs include two-dimensional (2D) nano-sheets which show a whole new range of properties when compared to their three-dimensional (3D) bulk equivalents, with the change in properties arising from quantum confinement and/or surface and interfacial effects.

Graphene[2,3] (2D nano-sheet) is often the inspiration and basis for most typical LDMs, capable of generating quantum confined materials with a unique set of properties.[4-8] Graphene has risen as a fascinating system in condensed matter physics not only in fundamental science but also technological applications.[2, 9] Graphene is a semimetal with band gap (E_g) closing at 0 K, which prohibits switching off the graphene channels in field-effect transistors and building functional junctions in graphene optoelectronics.[9] Efforts have been spent to create semiconducting graphene materials that preserve its unique transport property. Since the exceptional transport properties of graphene originate from its specific structure,[10] modification of the graphene lattice at the atomic level is necessary to modify its electronic properties. To this end, different schemes are proposed[11, 12] with some involving growing graphene on substrates,[13] doping[14-19] and/or introducing strain effects on the graphene surface,[20, 21] among others. Each experimental recipe has advantages as disadvantages, as recently discussed by Dvorak et al.[9]

Hexagonal boron nitride (*h*-BN) closely resembles elemental carbon structures by sharing the same total number of electrons between the neighboring atoms.[22-24] The structural similarities between graphene and a *h*-BN allow to form essentially seamless in-plane hybrids with continuously tunable BN:C stoichiometry.[23] Also two dimensional graphene and *h*-BN structures have become an important subject of research, owing to their mechanical strength and a rich variety of physical phenomena connected to their electronic structures.[2] *h*-BNC is an interesting structure that would enable tailoring of physical properties in graphene-based structures by varying the ratio of BN and C in these materials. *h*-BNC heterolayer structures were first prepared in the about 20 years ago.[25] All theoretical studies at various levels of theory[26-28] as well as experiments[29] indicate that for the BN and C regions it is energetically favorable to

Physical Chemistry Chemical Physics Accepted Manuscript

completely phase separate in *h*-BNC sheets. Composites of graphene and BN, usually referred to as $B_xN_yC_z$,[30] containing these elements in varying proportions can lead to *h*-BNC networks and photoluminescence measurements indicate that the gap appears to be smaller in carbon-rich samples.[31]

Obviously, synthesized graphene samples always contain defects of different types.[2, 32-34] Defects in graphene break the symmetry of the infinite carbon honeycomb lattice[35] and their nature and concentration depends on the preparation methods. Thus, it is important to study the different types of possible defects[36]. One usually distinguish between typical, almost self-defined, defects such as edges, grain boundaries, vacancies, implanted atoms, defects associated to a change of carbon-hybridization and more complex structures such as inverse Stone-Thrower-Wales defects,[37] hydrogen passivation,[38] boron and nitrogen doping,[39, 40] and nano-scale holes creating graphene nano-meshes.[41] Topological defects, defined as the introduction of non-hexagonal rings in the carbon lattice preserving the connectivity of the network, play a very important role in graphene and related nano-structures.[42] Among topological defects extended line defect structures provide a new set of building blocks for nano-materials that could lead to new physical effects and device concepts.[43] The study of the corresponding electronic and transport properties indicates that these linear defects behave as an effective inner third edge of the system and introduces a new channel for low energy electrons[35, 46] and, therefore, it is important to learn how to introduce these defects in controllable ways.**Error! Bookmark not defined.** The controlled engineering of these defects represents a viable approach to create and nano-scale control of one-dimensional charge distributions within widths of several atoms only.[44]

More recently, a bottom-up approach was used to create extended line defects (ELD) in graphene sheet.[45] Here, the extended line defect contains octagonal and paired pentagonal sp^2-hybridized carbon rings embedded in a perfect graphene sheet; the resulting structure being denoted as 585-ELD and this defect is precisely the origin of the one-dimensional metallic wire character of the resulting sheet.[45,46] Possible pathways for introducing ELDs involve implantation of C_2 clusters in the perfect lattice[47] or thermal annealing of the system with an array of atomic di-vacancies.[48] Nevertheless, adsorption is also expected to induce useful modifications of electronic properties of carbon based materials.[49] Based on density functional theory calculations, Li et al.[50] have suggested that linear adsorption of ad-atoms can form a 585-ELD as well as a N-doped 585-ELD.

Physical Chemistry Chemical Physics Accepted Manuscript

Clearly, *h*-BN and *h*-BNC sheets, like any other real materials, are likely to also contain structural defects.[28, 37, 51-54] These defects are often characterized by pentagonal, heptagonal or octagonal rings in the hexagonal lattice and can be introduced to alter their properties for suitable applications.[12, 33, 55-57] The physical properties of these defects and defect concentration have also been investigated in quite detail.[2, 28, 51, 58] In the case of monolayer *h*-BN, the possibility of band gap engineering by the introduction of zigzag-direction boundary has been recently considered.[59] Due to the importance of grain boundaries (GBs) in future applications of 2D sheets, theoretical models have been considered.[60-63] The effect of morphology and dopants on the 2D nano-material properties has also been investigated rather extensively.[14-18, 64-68] The effect of substitutional B or N doping and BN co-doping in the energetics and electronic properties of graphene with grain boundary defects have also been investigated[17] and the obtained results indicate that the GB region presents the energetically most stable impurity sites for the incorporation of single B or N atoms and also of the BN pair. First-principles calculations on the electronic and magnetic properties of hybrid BN nano-ribbons and sheets with both zigzag and armchair segments, which are joined by the 5−7 line defects, have also been recently reported[69] showing that the 5−7 line defects in hybrid BN ribbons reduce the band gaps of perfect *h*-BN systems, and that the hybrid BN nano-ribbons with two hydrogen-terminated zigzag B edge exhibit metallic → semiconducting → half-metallic behavior transitions as the number of zigzag BN chains increases.

The review of the literature above reveals that a structural modification with some embedded non-carbon atom chain (e.g., H, F, B, and N) is likely to allow one to tune the band gap of graphene samples. Composites of graphene containing B, N and C in varying proportions ($B_xN_yC_z$) can result in hexagonal BNC networks with tuned band gap.[30] Adsorption is also expected to induce useful modifications of electronic properties of carbon based materials. A class of 2D hexagonal graphene-like nano-structures such as embedded-line-defect in graphene is produced through this approach.[70] Inspired by adsorption method[50,71] and the experimental work of Lahiri et al.[45] suggesting the possibility of the line defect creation in graphene and that this leads to new and interesting electronic properties, we present a systematic theoretical study of this type of novel systems. To this end models of composite *h*-BN-graphene sheets (*h*-$B_xN_yC_z$) are constructed with 585-ELD and 5775-ELD defects.

Materials modeling

Physical Chemistry Chemical Physics Accepted Manuscript

Recently, based upon density functional theory based methods and molecular-dynamics simulation a model for the 585-ELD has been generated by the incorporation of a C_2 ad-dimer above opposing bridge sites on a hexagonal ring of carbon atoms of G sheet.[Error! Bookmark not defined.] Following this strategy, two kind of extended line defects with different ring size, namely 585-ELD and 5775-ELD, are generated in G and *h*-BN sheets (see schematic representation in Figure 1 and Figure 1S). The most significant difference between the procedure used to generate the 585-ELD and 5775-ELD is the site at which C_2 ad-dimers are adsorbed. To introduce pentagonal and octagonal rings on the G sheet, C_2 ad-dimers are added to every alternant hexagonal ring of the G sheet.[Error! Bookmark not defined.] The resulting 585-ELD structure, denoted as O-I (see also Table 1S) involves a pair of fused pentagons and one octagon rings.[Error! Bookmark not defined.] In the present work C_2 ad-dimers are also implanted in hexagon rings separated by two unmodified hexagon rings in the G sheet. The resulting structure now includes pentagonal and heptagonal rings in such a way that two pentagons are fused and contains a double heptagon ring. This is usually referred to as 5775-ELD or simply H-I as in Table 2S.

In the present work, periodic boundary conditions, both parallel and normal to the line defects, are used which cause the line defects to be periodically repeated in the G sheet. Because of the periodicity, the chain of C_2 ad-dimers implanted in the G sheet is parallel to a zigzag edge. In the obtained periodic models, zigzag nano-ribbon like structures are produced which embed the 585-ELD and 5775-ELD in the two dimensional G sheet. In a second step, the geometry of the initial structures is optimized by appropriate relaxation of the atomic positions and of the unit cell parameters as indicated in the next section. The C_2 ad-dimers in O-I and H-I structures interact with the G sheet to form a backbone for adjacent 5–8 and 5–7 membered rings, respectively. Since out-of-plane displacement of carbon atoms is easier than that within the plane, the structure buckles at the line defects to efficiently release the compression (Figure 1S). In the resulting energy optimized structure, all carbon atoms contribute to the π system which give the G sheet much of its interesting charge transport character. Nevertheless, analysis of the reconstructed structures show that when both the cell in the axial direction and the atomic positions are allowed to fully relax, the corrugated O-I structure transforms to a flat 2D sheet whereas the H-I structure remains corrugated. At this step, the cell parameter 'a' of the O-I structure increases by ~1.40 Å whereas the corresponding value for H-I structure just increases

Physical Chemistry Chemical Physics Accepted Manuscript

by ~0.11 Å. For the O-I and H-I structures, the C_2 ad-dimers bond length is ~1.44 Å and ~1.42 Å, respectively.

The strategy outlined above has also been used to generate reliable models for the 585-ELD and 5775-ELD in the *h*-BN sheet, the resulting structures are denoted as O-II and H-II, respectively (Figure1). Similar to the situation encountered in its isoelectric G sheet counterpart, the nano-ribbon like structure is generated in the defective *h*-BN sheet. Here it is worth to mention that incorporation of a BN moiety in *h*-BN sheet results in considerable tilting of the initial defective structure which is well visible in Figure 1. The corrugation is maintained upon relaxation of the atomic positions although relaxation of the cell parameters and atomic positions finally lead to two dimensional flat and corrugated structures for O-II and H-II, respectively (Figure 1). In the latter O-II structure, the cell parameter 'a' increases by ~1.77 Å but for the H-II structure the 'b' cell parameter just increases by ~0.13 Å. The added BN moiety directly binds to the substrate until a final relaxed bond length of ~1.47 Å is obtained for both O-II and H-II structures.

Composite *h*-BN-graphene sheets (*h*-$B_xN_yC_z$) can be also generated by adsorption of a BN moiety in varying proportions on pristine graphene and defective graphene sheets. These structures in principle provide the possibility of band gap engineering. Depending on the orientation of the interface relative to the crystallographic axis of the G sheet, two broad types of interfaces between the *h*-BN and graphene domains exist: an armchair-type interface (***A***) and a zigzag-type interface (***Z***). The ***A*** interface is perpendicular to the ELD local site and the ***Z*** interface is parallel to the ELD placement (Figure 2S). Therefore, two possibilities exist for BN-doping in O-I and H-I structures; one from ***A*** interface and the other from ***Z*** interface. For this reason we designate the BN-doped ELDs superlattices with rectangular shape as *h*-$B_xN_yC_z$, where x, y and z denote the number of B, N and C atoms, respectively. Similarly, the resulting superlattices are denoted as ***A***-$B_xN_yC_z$ and ***Z***-$B_xN_yC_z$ where, as mentioned above, the difference between ***A***-$B_xN_yC_z$ and ***Z***- $B_xN_yC_z$ derives from the BN-doped model at the ***A*** and ***Z*** interfaces.

For these four possibilities, namely ***A***-$B_xN_yC_z$-585 ELD, ***Z***-$B_xN_yC_z$-585-ELD, ***A***-$B_xN_yC_z$-5775-ELD and ***Z***- $B_xN_yC_z$-5775-ELD, different percentage of BN moieties is inserted. Note also that, in all different BN-doped ELDs one has x=y. By considering the two ***A*** and ***Z*** interfaces and different percentages of BN moiety 19 different structures have been generated and their structure optimized. A summary of results is reported in Tables 1S and Table 2S where, for

Physical Chemistry Chemical Physics Accepted Manuscript

simplicity, the abbreviated notation for each structure is used. Figure 2 and Figure 3 show the full relaxed unit cells, relative stability and band gaps of all mentioned structures.

To further clarify the issue we describe in detail the construction of different ***A***-$B_xN_yC_z$-585-ELD structures. Doping the O-I unit cell with 34 carbon atoms is carried out in 5 steps. In each step 8 carbon atoms of O-I structure are replaced with 4 BN moieties. The additional step being related to doping of C_2 ad-dimers in the O-I structure. Table 1S shows the unit cell of all fully relaxed G-585-ELD (O-I,) ***A***-$B_4N_4C_{26}$-585-ELD (OA-I), ***A***-$B_5N_5C_{24}$-585-ELD (OA-II), ***A***-B_9N_9 C_{16}-585-ELD (OA-III) and ***A***-$B_{13}N_{13}C_8$-585-ELD (OA-IV) structures. A similar approach was applied to build different BN doped defect-free graphene sheets (Table 3S and Table 4S).

Computational details

First-principles calculations have been performed using the density-functional theory (DFT) scheme implemented in the PWSCF code of the Quantum ESPRESSO suite.[72] The generalized gradient approximation (GGA) exchange-correlation density functional[73] was employed together with plane wave (PW) basis set, ultrasoft pseudopotentials (US-PP) ,[74, 75] and a kinetic energy cutoff of 460 eV. The graphene (*h*-BN or composite *h*-BN-graphene) supercells with 585-ELD and 5775-ELD contains 34 and 50 B/N/C atoms, respectively. Defective composite *h*-BN-graphene supercells differ in the size and in the arrangement of BN and graphene domains are shown in Figure 2 and Figure 3. For Brillouin zones (BZ) integration, we have used a Γ-centered Monkhorst Pack[76] scheme with different *k*-meshes depending on the BZ dimensions. Accordingly we have used $2 \times 5 \times 1$ and $3 \times 5 \times 1$ *k*-points meshes during the geometry optimization for the all supercells including 585-ELD and 5775-ELD, respectively. The energy convergence for all electronic steps was set at 10^{-8} atomic unit.

Periodic 2D boundary conditions are considered along the growth directions of the sheets, and a sufficiently large vacuum spacing of 20 Å in perpendicular direction of surface was used to prevent unwanted interactions between adjacent layers. To obtain a stable configuration, structural relaxations were performed in two steps without any symmetric constraint. In the first step the atomic positions are allowed to fully relax and in the second step both the cell along the growth directions of sheets and the atomic positions are allowed to fully relax until the forces acting on each atom are smaller than 0.001 eV/Å. It is important to keep in mind that the ~ 1.8 % mismatch between the cell parameters of graphene and *h*-BN sheets implies that, after full relaxation, the different systems studied exhibit different cell parameters. Such two-step

Physical Chemistry Chemical Physics Accepted Manuscript

optimization setup is adequate for modeling defects and doped impurities in 2D systems with covalent bonding.

All optimized structures were further characterized as local minima in the potential energy surface by a proper vibrational frequency analysis. This analysis carried out by the numerical calculation and diagonalization of the Hessian matrix, constructed from finite differences of analytical gradients. The elements of the Hessian matrix have been obtained by calculating energy changes due to independent displacements of every atom in the system by 0.03 Å in each direction of the unit cell vectors. In order to calculate transmission, the maximally localized Wannier functions (MLWFs) centers for occupied σ bands are chosen at every bond center and the centers of the MLWFs for π bands are considered on every B/N/C atoms for the candidate structures.

To investigate the stability of the proposed structures we rely on the cohesive energy defined as[77]:

$$E = (-E_{B_xN_yC_z} + xE_B + yE_N + zE_C)/Nat, \quad (1)$$

where $E_{B_xN_yC_z}$, E_B, E_N and E_C are the total energies of the composite *h*-BN-graphene systems, free B, N, and C atoms, respectively, and x, y, and z are the number of B, N, and C atoms in the supercell, respectively, and Nat stands for the total number of atoms in the supercell. Finally, the electrostatic potential surface, EPS, was calculated in order to explore intramolecular properties such as the charge distribution, which shows how the reactivity of the pristine G is affected by the coexistence of extended line defects and BN moiety doping.

To evaluate the adequacy and accuracy of the computational procedure outlined above, structural and electronic properties of pristine G and *h*-BN sheets have been computed and band structures, density of state (DOS), projected density of state (PDOS) on atoms, valence band edge state (VBES), conduction band edge state (CBES) and EPS have been obtained (see Figure 3S). The optimized bond length of graphene (1.42 Å) and of *h*-BN sheets (1.45 Å) are in good agreement with the experimental results of 1.42 Å for graphene and of 1.44±0.1Å for *h*-BN monolayer[78]. The analysis of cohesive energy values shows that graphene (8.98 eV/atom) is more stable than a *h*-BN monolayer (8.6 eV/atom), in agreement with previous theoretical values.[77]

Although the two ideal structures are isoelectronic, their electronic properties are, not unexpectedly, quite different. The shapes of the VBES and CBES states of G sheet are

Physical Chemistry Chemical Physics Accepted Manuscript

symmetrical but in the *h*-BN sheet, due to different electronegativities of B and N atoms, the shapes of the VBES and CBES states are asymmetrical (see inset of Figure 3Sa and Figure 3Sb). Such a special characteristic of *h*-BN monolayer results in the opening of a large energy gap. The DOS in Figure 3Sc shows that pristine G behaves like a zero-band-gap semiconductor whereas the calculated band gap of a *h*-BN sheet is 4.65 eV which, again, is in agreement with previous theoretical works,[79] but it is smaller than the 5.97 eV value obtained from experiments on bulk *h*-BN[80] which is to be expected from the well-known trends in band gaps predicted by GGA functionals.

The electrostatic potential surface of pristine G and a *h*-BN sheets mapped onto electron density with isodensity values of 0.04 a.u. (Figure 3Se and Figure 3Sf). The regions of pristine G sheet with negative EPS actually reveal the sigma bonding between C-C atoms whereas the positive regions display π system. The calculated EPS of pristine *h*-BN monolayer (Figure 3Sf) shows that charge densities are clearly separated, indicating that there is no resonance effect.

Results and discussion

Atomic and electronic structure of 585 and 5775 defective graphene

Following the idea of the construction of extended line defects in graphene, we first discuss the results for fully relaxed O-I and H-I structures. Within the unit cells employed to represent each systems, the calculated cohesive energy of O-I structure (~8.83 eV/atom) is lower than for H-I structure (~8.88 eV/atom) and not too far from the corresponding value for graphene (8.99 eV/atom) thus reflecting the strong stability of these ELDs. Note, however, that the present calculations predict H-I structure to be about 0.05 eV/atom more stable than O-I structure which has been synthesized[45]. The structural stability of these structures has been confirmed by pertinent frequency calculations. The full relaxed geometry of the O-I and H-I structures as predicted from the DFT based calculations are shown in Figure 2 and Figure 3. Even if G keeps its planar structure after implantation of the 585-ELD, the geometry optimization showed that when C_2 ad-dimers incorporate above opposing bridge sites on a hexagonal ring of carbon atoms, the G surface becomes distorted and pentagon, hexagon and octagon regions are forming in the sheet parallel to zigzag edge (Figure 1S). Due to the fault growth, the bond angles at the O-I structure are changed to ~141.97°, ~136.30°, ~125.42° in octagon and ~109.01°, 104.71° and 112.55° in each pentagon rings. The C-C bond lengths around the 585-ELD elongate from 1.39Å to 1.47Å in different rings, which is still comparable to the bond length of 1.42 Å of C-C in

Physical Chemistry Chemical Physics Accepted Manuscript

pristine G. These values further indicate that all the carbon atoms show C–C bond lengths and angles that consistent with a sp^2 hybridization. For the relaxed H-I structure, the dihedral angle for C–C double bonds becomes nonzero; the perpendicular spacing between the highest and lowest carbon atoms being of ~2.7 Å. Other structural results are rather similar to those found in O-I structure. To investigate the effect of 585-ELD and 5775-ELD on the electronic properties of graphene, the calculated band structure, DOS, EPS, VBES and CBES stats of the O-I and H-I structures have been obtained and analyzed (Figure 4a-4i). Although both O-I and H-I structures consist of sp^2 (three-fold coordinated) C atoms, the electronic structure of the extended line-defective graphene is remarkably different from that of a defect-free G sheet. As can be seen from Figure 4a, the O-I conduction band flattens around the Γ point, in the center of the O-I structure Brillouin zone, which is not observed in the case of H-I structure (Figure 4c). As reported in previous work,[71] this flat band of O-I structure is empty. In order to confirm the empty character of the flat-band state around the Γ point we have calculated the quantum conductance of O-I and H-I structures from Γ to X high symmetry points using the MLWFs (Figure 4S). Our calculations show that, because of positioning the empty flat band around Γ point at the Fermi level, the quantum conductance in O-I structure is zero. In contrast the conductivity of H-I structure around Γ point at the Fermi level is not zero as expected from the lack of the flat band.

Previous computational studies reported that monolithic ridge of defects could be used to influence the direction of charge transport eventually leading to nanowires in graphene-based electronics.[37, 55] The analysis of the charge density distribution at the Fermi level reveals a directional localized and delocalized form for O-I and H-I structures, respectively. Accordingly the localized nature of embedded 585-ELD in monolithic G sheet generates a perfect one-dimensional metallic wire. In contrast to the O-I structure, delocalized nature of H-I states lead to a non-directional two dimensional metallic defective G sheet. Contrary to O-I structure where the 585-ELD has metallic nanowire character, 5775-ELD in the graphene sheet causes peculiar metallic nanosheet for the H-I structure. This point of view is reinforced from the VBES and CBES of O-I and H-I structures displayed in Figure 4g and Figure 4i.

To further analyze the electronic structure features of these ELDs, the EPS of O-I and H-I structures (Figure 4b and Figure 4d) are compared to that of G (Figure 3Se) sheet. The similarity in the EPS for these three structures is consistent with the sp^2 hybridization of carbon atoms. A

Physical Chemistry Chemical Physics Accepted Manuscript

similar comparison between the DOS of G, O-I and H-I structures at the Fermi level (Figure 4f) shows that accessible density of states at the Fermi level for the O-I structure is higher than the H-I one; in other words, the O-I structure has more metallic character than the H-I one. Qin and et al.[81] found that the main contributions to the states around the Fermi level originate from the C(2p) orbitals at the line defect with negligible contribution from atoms which are far away from the defect which is in agreement with the finding of Lahiri et al.[45] These findings are consistent with present results are illustrated by the PDOS for 2p orbitals of all C atoms of O-I and H-I structures at the Fermi level which are shown in Figure 5a and Figure 5b, respectively. The implications of these results are that incorporated C_2 ad-dimers, which are located along the line defects, have major participation in metallic behavior of the O-I and H-I structures. This observation confirms the localized and delocalized nature of the charge density distribution in the O-I and H-I surfaces, respectively (Figure 5a and Figure 5b).

Atomic and electronic structure of 585 and 5775 defective *h*-BN

Similar to previous section, the 585-ELD and 5775-ELD are embedded in the *h*-BN sheet by incorporation of a BN moiety. This becomes possible simply by positioning the BN moiety every two or three periods of the of *h*-BN monolayer above opposing bridge sites on a hexagonal ring as above described (Figure 1). Unlike in the case of pristine G sheet, the symmetry of the heteroatomic unit cell of *h*-BN monolayer sub-lattice is broken and, as a result, the 585-ELD and 5775-ELD embedded structures are asymmetric too (for simplicity this kind of defect embedded structures are denoted as O-II and H-II as in Table 1S and Table 2S, respectively). Both, O-II and H-II structures terminations have N-rich and B-rich zigzag edges (Figure 2Sc and Figure 2Sd). The O-II structure is composed of one asymmetric octagon ring which includes B-B and N-N homopolar bonds and six B-N bonds. The optimized bond length of homopolar B-B and N-N are 1.66Å, 1.45Å, respectively whereas those of the six B-N bonds are in the 1.42-1.49 Å range. The bond angles of the asymmetric octagon ring vary between 124°-143°. This asymmetric octagon ring causes the four linked pentagon rings to be asymmetric too (Figure 2Sc and Figure 2Sd). Note, however, that the four pentagon rings have different atomic environment. In H-II structure, two heptagon rings are different, one of them having one B-B homopolar bond and six B-N bond with bond length of 1.63Å and 1.43-1.52Å, respectively, and the bond angles being in the 116°-130° range, all consistent with sp^2 hybridization. The other heptagon ring consists also of one N-N homopolar bond and six B-N bonds but the former has 1.44Å bond-length and the latter are in

Physical Chemistry Chemical Physics Accepted Manuscript

Physical Chemistry Chemical Physics Accepted Manuscript

the 1.44-1.52Å range as in the first heptagon. This is also the case for the bond angles which are in the 120-131° interval. It is clear that asymmetry causes the four connected pentagons to be structurally different.

The analysis of the electronic structure can be easily carried out from the band structure, DOS, VBES and CBES plots of O-II and H-II structures depicted in Figure 6. The DFT based method predicted band gaps show significant differences with respect to the case of the pristine *h*-BN sheet. Here, the generation of some corrugated and/or flat bands near the Fermi region of O-II and H-II band structures implies that the direct 4.65 eV band gap of pristine *h*-BN sheet can be tuned to indirect band gap of 2.75 and 3.21 eV in O-II and H-II structures, respectively. Hence, the present model calculations predict that 585-ELD and 5775-ELD embedded in pure *h*-BN sheet transforms the insulator character of the pristine *h*-BN sheet; which is suitable for ultraviolet adsorption, to clear semiconducting materials which are suitable for visible-light and ultraviolet adsorption regions, respectively. The valence and conduction band edge states of the O-II and H-II structures in DOS illustrate the reduction of band gap of these ELDs with respect to pristine *h*-BN sheet (Figure 6f). This means that the charge transport character of these structures is enhanced.

Compared to the delocalized nature of the VBES and CBES states of pristine *h*-BN sheet in which VBES states placed on N atoms and CBES states placed on B atoms, the VBES and CBES states of O-II and H-II structures are localized across the ELDs. Therefore, these kind of line defects cause the generation of perfect one-dimensional semiconductor wires with different properties, embedded in the perfect *h*-BN sheet. The contribution of B and N (2p) orbitals of the O-II and H-II structures to gap opening is clear from the corresponding PDOS. Figure 7 shows that the incorporated BN moiety 2p orbitals, located along the line defects in both O-II and H-II structures, have a minor portion in semiconductor character of systems.

Regarding the stability, DFT based calculations show that, in spite of homopolar (B-B and N-N) bond frustration in O-II and H-II structures, the cohesive energy of the O-II and H-II structures — ~8.47 eV/atom and ~8.46 eV/atom, respectively — are still close enough to the ~8.60 eV/atom value for pristine *h*-BN sheet. The prediction of two structures with nearly similar stability and different band gaps provides opportunity for application in different electronic devices.

Structural and electronic properties of 585 and 5775 defective *h*-BNC

Encouraged by the idea of finding a potential application for the ELDs, we consequently extend the investigation to G with potential sub-lattice symmetry breaking by BN-doping. The preparation of BN-doped defective G sheets with two ***A*** and ***Z*** interfaces have already been described in the material modeling section. Here we recall that 19 different structures exist with different percentages of B, N and C atoms. The ring labels of the 34-atoms unit cell for O-I and 50-atoms unit cell for H-I structures are depicted in Figure 2Sa and Figure 2Sb, respectively. From the figures it is clear that symmetry breaking of O-I and H-I structures by BN doping in two ***A*** and ***Z*** directions is likely to introduce vivid changes in electronic and structural properties. To verify that this is the case, we calculated the length of the circumference (L_c) circumscribing (Figure 2Se) all rings in BN-doped O-I and H-I structures. This structural quantity can provide useful information on the properties of doped moieties in ***A*** and ***Z*** directions. Note that, as a consequence of mirror symmetry in both O-I and H-I structures, the rings that are symmetrical relative to the line defects axis have the same circumference in both O-I and H-I structures (Figure 5S). A detailed investigation of the L_c values for defective and doped structures in two ***A*** and ***Z*** interfaces shows a particular regularity between L_c values in these two directions. This regularity is displayed in Figure 8 for four ***A***-BN-doped O-Is, ***Z***-BN-doped O-Is, ***A***-BN-doped H-Is and ***Z***-BN-doped H-Is. To better understand the information provided by L_c, let us have a close look to the observed regularity for all armchair and zigzag BN-doped 585 ELDs. When BN-doping starts from the ***A*** direction the trend in L_c shows a correlation following the (1→14) , (2→15), (3→12), (4→13), (5→10) and (6→11) sequence (Figure 8a) where the numbers in this sequence are taken from the ring labels in Figure 2S. Likewise, when BN-doping starts from the ***Z*** direction, the correlation sequence is (1→2), (3→4), (5→6), (10→11), (12→13) and (14→15) (Figure 8b). In the latter and former cases correlated rings are parallel and perpendicular to the extended line defect orientation, respectively. This observation indicates that replacement of C atoms by a BN moiety in both O-I and H-I structures in ***A*** (***Z***) direction induces a correlation between the rings in the ***A(Z)*** directions. In order words, in spite of C-C substitution by BN moiety, the long range symmetry is maintained.

To inspect the relative stability of the BN-doped ELD structures, the cohesive energy values have been calculated as in Equation 1 and plotted in Figure 2 and Figure 3 taking that of G sheet as reference. The plots in these figures reveal that, among the nineteen studied structures, O-I and H-I are the most stable structures. Increasing the fraction of BN moiety up to ~75%

Physical Chemistry Chemical Physics Accepted Manuscript

Physical Chemistry Chemical Physics Accepted Manuscript

atoms of supercell (OA-IV and OZ-III of Figure 2 and HA-III and HZ-IV of Figure 3) leads to decrease in stability. However, replacement of all atoms in ***A*** directions leads to a structure (O-II of Figure 2 and H-II of Figure 3) which is more stable than the defective composite *h*-BN-graphene sheet with 75% BN atoms. However, stability decreases for the full replacement of atoms in the ***Z*** direction. Intermediate geometries in both cases can be regarded as being metastable doped and defective structures. This is not unexpected since the atomic arrangement with the lowest formation energy have strong preferences for C–C and B–N bonds whilst are unfavorable for B–C, C–N, B–B, and N–N ones.[82] The stability transition as a function of B and N chemical potentials has been reported by Gomes et.al.[83] These authors predict that fine tuning the chemical potentials may lead to the structures with low stability,[83] a result which may pave the road to production of the intermediate metastable structures analyzed in the present work. In general the ***Z***-BN-doped O-I and H-I structures are more stable than ***A***-BN-doped O-I and H-I structures.

The predicted band gaps for all BN-doped O-I and H-I structures are also collected in Figure 2 and Figure 3. The O-I and H-I structures have already metallic character with a zero band gap. The capability of BN moiety to tune the band gap of graphene was confirmed many times starting from the pioneering work of Giovannetti et al.[13] long time ago. However, to investigate the behavior of embedded C_2-addimers in BN-doped graphene sheets is also necessary. When ~25 (~60) % of carbon atoms of O-I (H-II) structure are replaced by BN moieties in ***A*** direction, OA-I (HA-II), the band gap goes to 0.78 (1.12) eV. When the incorporated C_2 ad-dimers, which are located along the line defect, are replaced by BN moiety leading to OA-II (HA-III) structure, the band gap further raises to 1.11 (1.19) eV. It means that due to this structural transformation (OA-I to OA-II) or (HA-II to HA-III) a band gap opening exists. In contrast, increasing the fraction of BN moieties -~0.50 (~50) %- of carbon atoms of O-I (H-I) structure in ***Z*** direction, OZ-II (HZ-II), the band gap goes to 0.00 (0.17) eV. In this structure when the incorporated C_2 ad-dimers, are replaced by BN moiety (leading to OZ-III (HZ-III) structure), the band gap goes 0.00 (0.16) eV. It means that due to this structural transformation (OZ-II to OZ-III) or (HZ-II to HZ-III) there is not clear band gap variation. In other words, the behavior of embedded C_2 ad-dimers in BN-doped graphene sheets strongly depends on the BN doped moiety in A or Z direction. When the BN-doped neighboring atoms of defective structures are in the A direction, BN doped of embedded C_2-addimers causes a band

gap opening, but when the BN-doped neighboring atoms of defective structures are in Z direction, BN doped of embedded C_2-addimers does not have a clear effect into the band gap opening. Obtained results show that the gap opening of O-I and H-I structures due to BN doping is closely correlated with doping direction in ***A*** or ***Z***. In general, the gap opening in ***Z*** direction is smaller than in ***A*** direction and independent of the defect. This is clear from the comparison of the structures with the same defect content in ***A*** and ***Z*** directions.

To clarify the coexistence of dopants and defects we have performed a detailed analysis of the individual role of the dopants and defects. In this respect, a set of calculations has been carried out on defect free BN-doped graphene sheets. Figure 6S and Figure 7S show the optimized unit cells, relative stability and band gap of the later structures. Obtained results are compared with the results of the defective BN-doped graphene sheets. A comparison of the individual effects clearly indicates that the trend in band gap changes and stability of defect free BN-doped graphene sheets are practically identical to defective BN-doped graphene sheets. A net effect of doping in the direct band gap opening of the defect-free graphene sheets by doping in both ***A*** and ***Z*** directions is clearly observed. Obvious differences are related to the type and extent of band gap opening. To illustrate the differences we have selected eight defect-free and defective structures with the same BN content (Figure 9 and Figure 10). Analysis of the selected defect-free and 585 defective BN doped graphene sheets in ***Z*** or ***A*** direction reveals that the existence of defects in BN-doped graphene sheet induces a reduction of the band gap with respect to the defect-free BN-doped graphene sheet and the change of direct band gap to indirect gap (Figure 9). A similar trend exist in the 5775-ELD but in this case by increasing the concentration of BN doping there is not explicit direct-indirect gap variation (Figure 10).

Conclusions

In the present work density functional theory based calculations and suitable models have been used to examine the coexistence of dopants and defects in graphene (G) and graphene-like *h*-BN sheets. The most stable structures have been determined by full geometry optimization on periodic slab models featuring embedded 585 and 5775 extended line defects in G (O-I and H-I structures, respectively) and a series of structures with different content of BN. Defective structures have been generated by introducing C_2 ad-dimers (BN moiety) to the G (*h*-BN) sheet in two different positions. The C_2 ad-dimers (BN moiety) show a high tendency to embed into

Physical Chemistry Chemical Physics Accepted Manuscript

the G (*h*-BN) sheets and the resulting two one dimensional extended line defects contain double pentagon–octagon rings (O-I structure) and double pentagon–double heptagon rings (H-I structure) with flat and corrugated structures, respectively. 5775-ELD in G sheet exhibits delocalized VBES and CBES across the sheet near the Fermi level. Therefore H-I structure is classified as metallic nano-sheet.

To the best of our knowledge there is no information about the electronic properties of the embedded 585-ELD and 5775-ELD in *h*-BN sheet. Nevertheless, the present calculations indicate that O-II and H-II structures are semiconductors with 2.76 and 3.22 eV indirect band gap, respectively. In comparison with the pristine *h*-BN the band gap of O-II structure is shifted towards the visible region whereas that of H-II structure reaches the ultraviolet region. The analysis of the VBES and CBES around the Γ point shows a localization region across line defects for both O-II and H-II structures. Therefore O-II and H-II structures classified as semiconductor nano-wires with different band gaps. A deeper inspection of the electronic properties reveals that in the transition from semimetal in G to metal in the defective G (O-I and H-I) sheets, the incorporated C_2 ad-dimers along the extended line defects play a crucial role. In a similar way, BN moieties along the extended line defect have essential role in the transition from insulator (*h*-BN sheet) to semiconductor (O-II and H-II structures) character.

Extensive analysis of the BN doped defective G (O-I and H-I) sheets with different BN concentration reveals different properties of these systems in the ***A*** and ***Z*** doped interfaces. By doping in the ***A*** (***Z***) direction the symmetry of the pristine defective graphene sheets are affected in vertical (horizontal) direction which is the cause to altered electronic properties. Accordingly, BN doped O-I and H-I structures in to ***A*** and ***Z*** directions yield metallic or semiconducting behavior with a band gap in the 0.00-2.76 eV and 0.21-3.22 eV range, respectively.

The calculated cohesive energy values for O-I and H-I structures indicate a strong stability, although the result show that H-I structure is about 0.05 eV/atom more stable than O-I. Interestingly, the less stable O-I form has been produced experimentally[45] which provides a bright prospect to experimental synthesis of H-I structure in the future. In addition, the cohesive energy per atom of all fifteen BN-doped structures (with a specific percentage and direction of interface between BN and G sheets) show that the relative stability of BN-doped ELDs decrease when the BN concentration becomes ~75% and that, in both O-I and H-I structures, the ***Z***-BN-doped structures are more stable than the ***A***-BN-doped ones. It is interesting to note that it has

Physical Chemistry Chemical Physics Accepted Manuscript

Physical Chemistry Chemical Physics Accepted Manuscript

been suggested that fine tuning of the B and N chemical potentials may lead to the structures with low stability,[83] a result which may pave the road for producing the intermediate metastable structured studied in the present work.

It should be emphasized that 585-ELD and 5775-ELD cause an increase in charge transport property or on the other word band gap reduction. And BN dopants cause to increase the bans band gap which is well known behavior for this dopant in graphene sheet. Coexistence of these phenomena and their mutual interactivity are behind the appearance of an average value for the band gap in comparison with the individual band gaps. Finally it can be concluded that mutual cooperation of dopants and defect tune the band gaps towards lower values and change the direct band gap to indirect regardless of dopant concentration in 585-ELD structures. However, in the 5775-ELD structures the change from direct to indirect gap depends on the dopant concentration. These results indicate the need for further studies with larger and diverse sheets, these are necessary to find an extended model for the dopant-defect correlation.

Acknowledgements

The authors are indebted to Dr. Francesc Viñes for carefully and critically reading the manuscript. F. N. is grateful to the Institute for Advanced Studies in Basic Sciences, for financial support. The research of F. I. has been supported by Spanish MICINN through research grant CTQ2012-30751, Generalitat de Catalunya grants 2014SGR97 and XRQTC and through the 2009 ICREA Academia Award for Excellence in University Research.

Physical Chemistry Chemical Physics Accepted Manuscript

Figure Legends

Figure 1. Top and side views models of initial, relaxed atomic positions and full (atomic position and cell parameters) relaxed structures of BN moiety linear adsorption on *h*-BN sheet for embedded 585-ELD (a, b, c) and 5775-ELD (d, e, f) structures, respectively.

Figure 2. Relative cohesive energy per atom with respect to graphene sheet with the same atomic content, band gap and full relaxed unit cells of O-I structure and its different BN-doped structures in two ***A*** and ***Z*** directions.

Figure 3. Relative cohesive energy per atom with respect to graphene sheet with the same atomic content, band gap and full relaxed unit cells of H-I structure sheet and its different BN-doped structures two ***A*** and ***Z*** directions.

Figure 4. Electronic band structures of (a) O-I and (c) H-I structures, EPS plots mapped onto electron density values with isodensity values of 0.004 a.u. of (b) O-I and (d) H-I structure, VEBGS of (e) O-I and (g) H-I structures, CEBS of (h) O-I and (i) H-I structures, respectively, (f) The total density of states for O-I, H-I, and G structures, respectively.

Figure 5. Magnitude of projected density of state of 2p orbitals of C atoms at the Fermi level for (a) O-I and (b) H-I structures, respectively. The highlight bars in plot are corresponding with highlight atoms in the unit cell.

Figure 6. Electronic band structures of (a) O-II and (c) H-II structures, EPS plots mapped onto electron density values with isodensity values of 0.004 a.u. of (b) O-II and (d) H-II structures, VEBS of (e) O-II and (g) H-II structures, CEBS of (h) O-II and (i) H-II structures, respectively, (f) The total density of states for O-II, H-II, and G structures, respectively.

Figure 7. Magnitude of band gap in projected density of state of 2p orbitals of B and N atoms around the Fermi level for (a) O-II and (b) H-II structures, respectively. The highlight bars in plot are corresponding with highlight atoms in the unit cell.

Figure 8. L_c variation as a function of different rings of O-I and its BN-doped structures in (a) ***A*** and (b) ***Z*** directions. L_c variation as a function of different rings of H-I and its BN-doped structures in (c) ***A*** and (d) ***Z*** directions.

Figure 9. Electronic Band structure of a) PA1, a1) OA-I, b) PZ1, b1) OZ-III structures, respectively.

Figure 10. Electronic Band structure of a) PA1‘, a1) HA-I, b) PZ2‘ and b1) HZ-III structures, respectively.

Physical Chemistry Chemical Physics Accepted Manuscript

Figure 1.

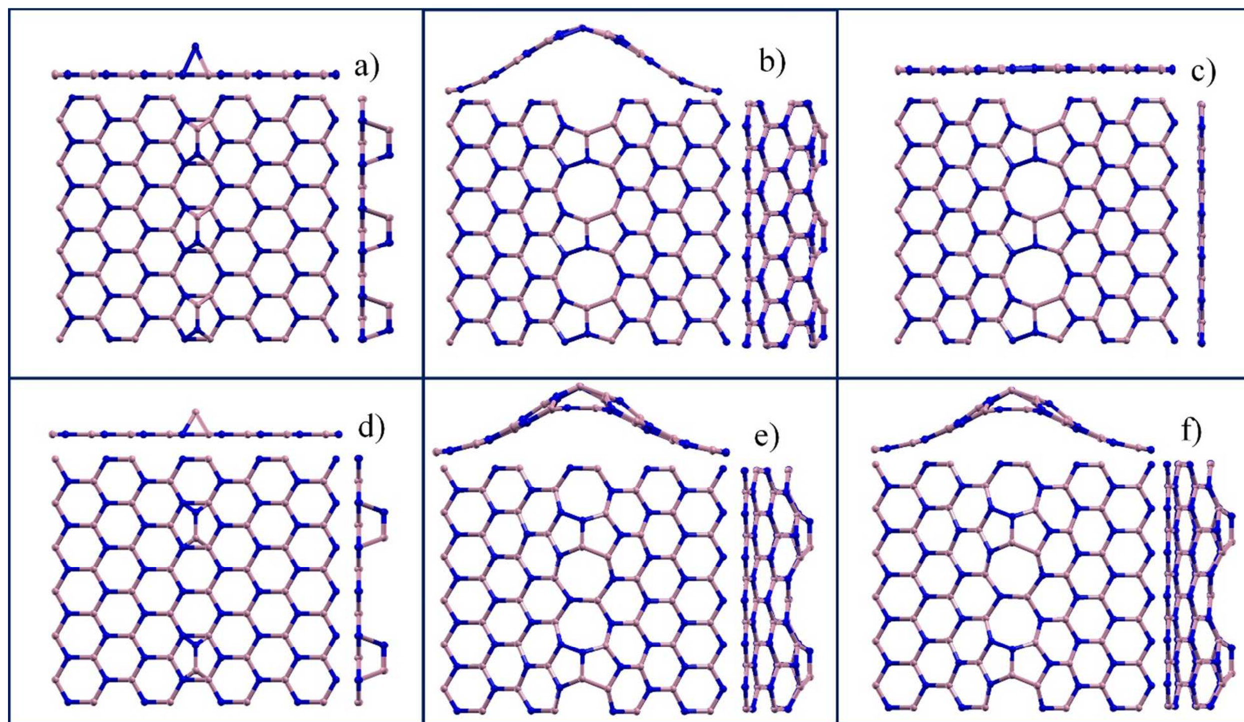

Physical Chemistry Chemical Physics Accepted Manuscript

Figure 2.

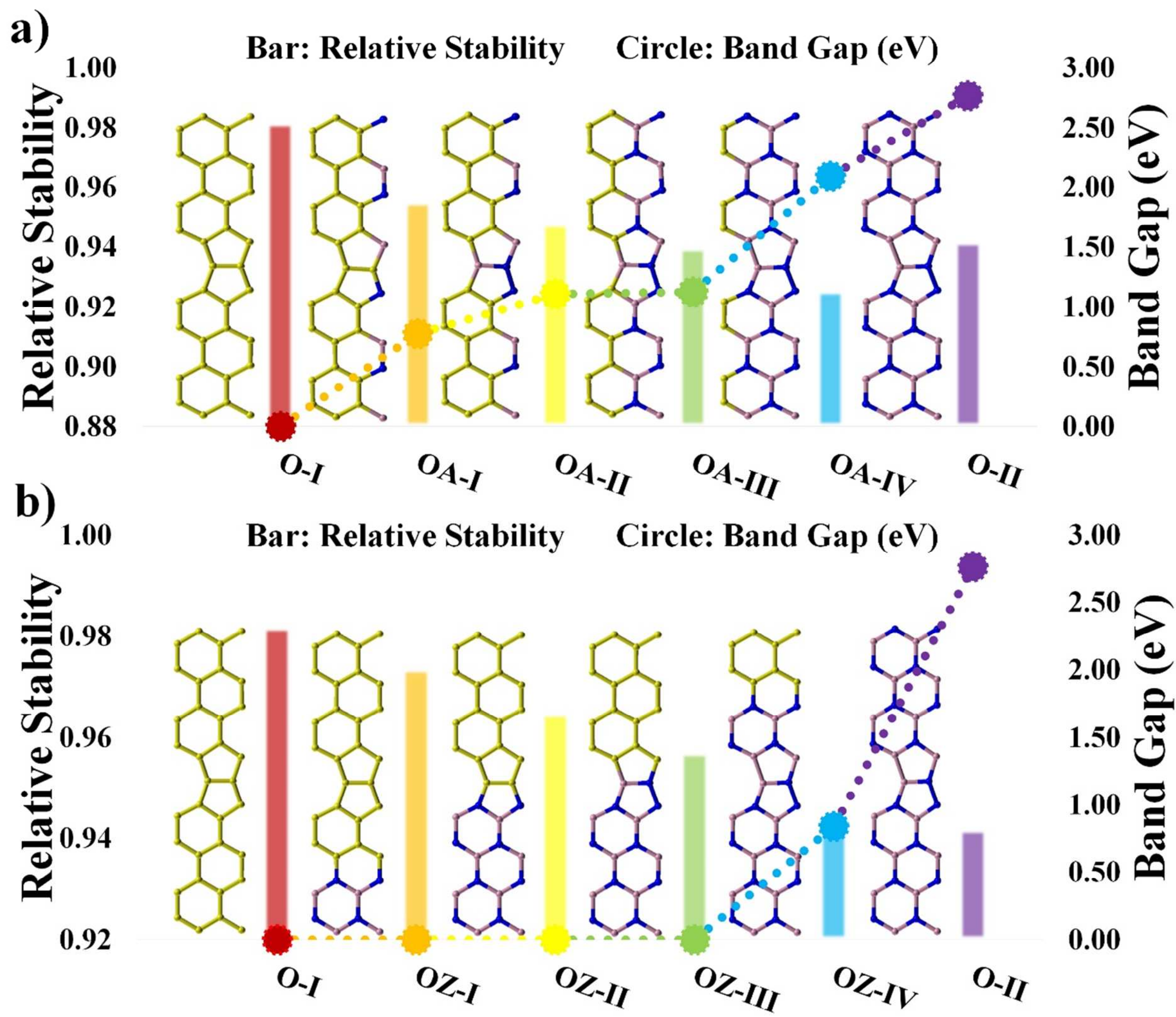

Physical Chemistry Chemical Physics Accepted Manuscript

Figure 3.

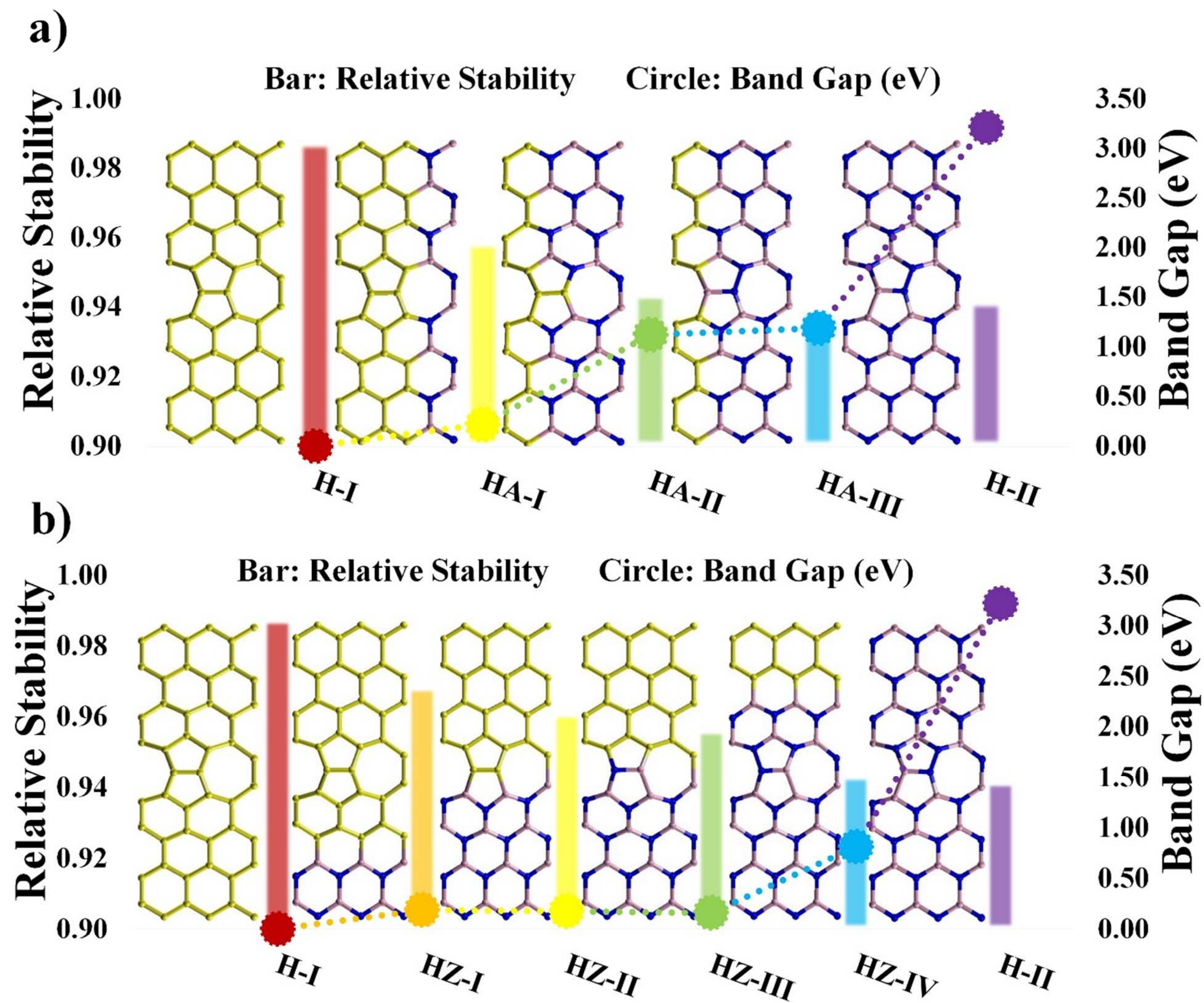

Physical Chemistry Chemical Physics Accepted Manuscript

Figure 4.

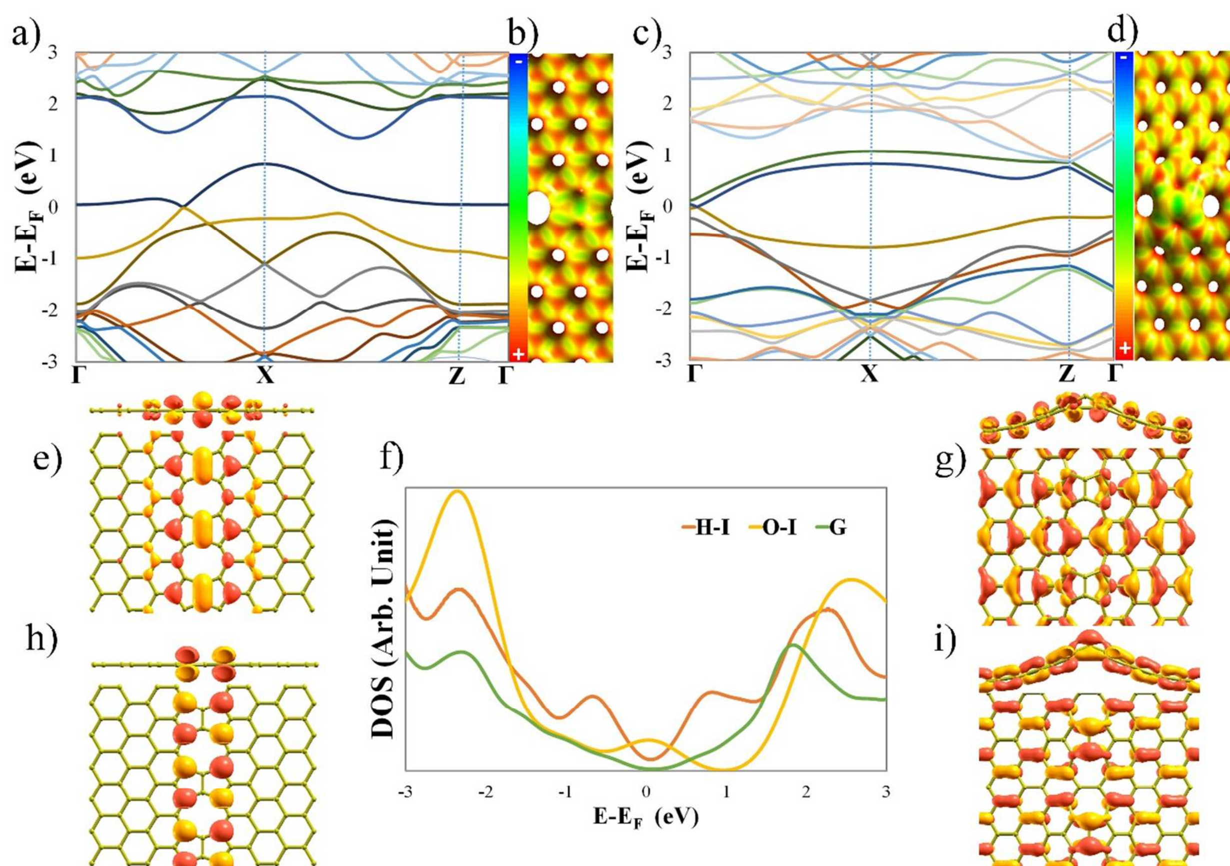

Physical Chemistry Chemical Physics Accepted Manuscript

Figure 5.

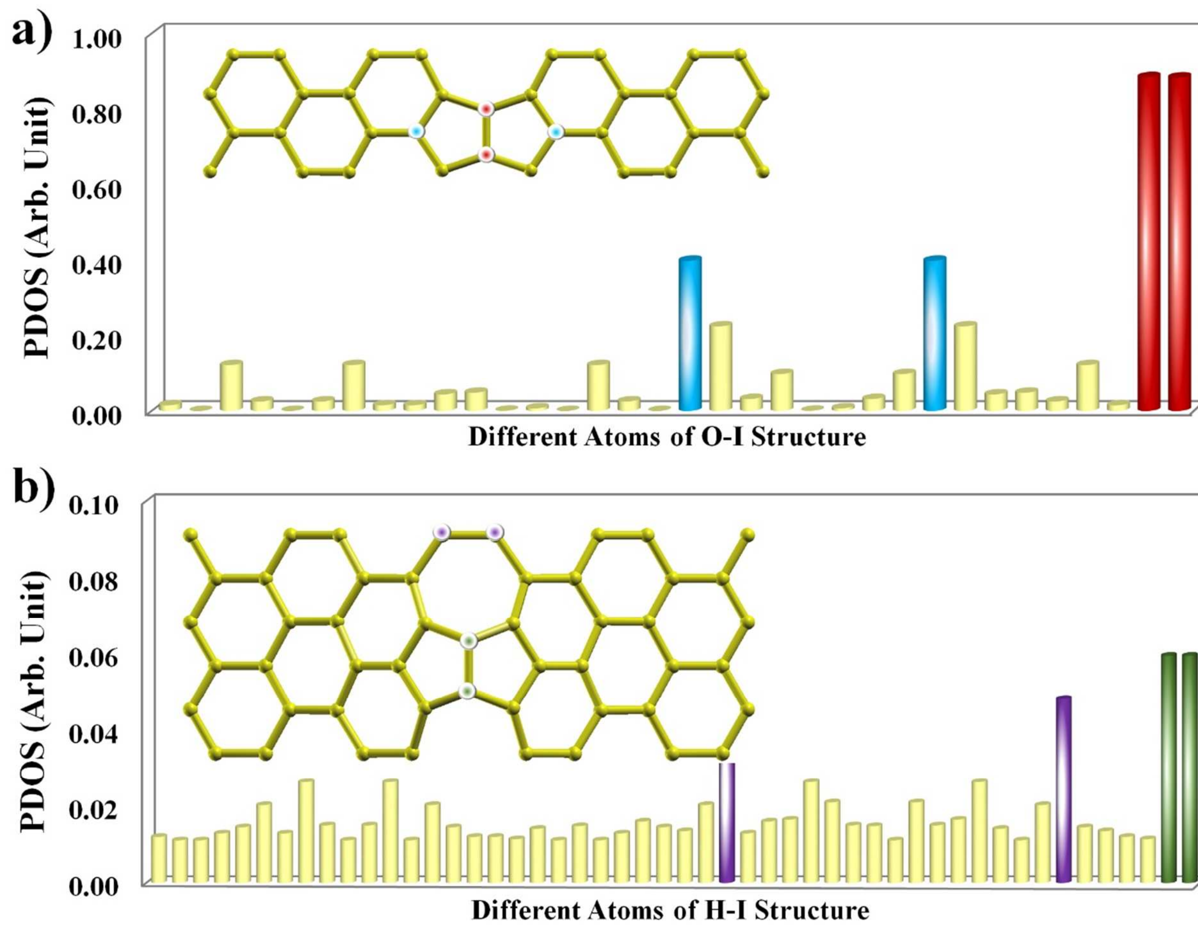

Physical Chemistry Chemical Physics Accepted Manuscript

Figure 6.

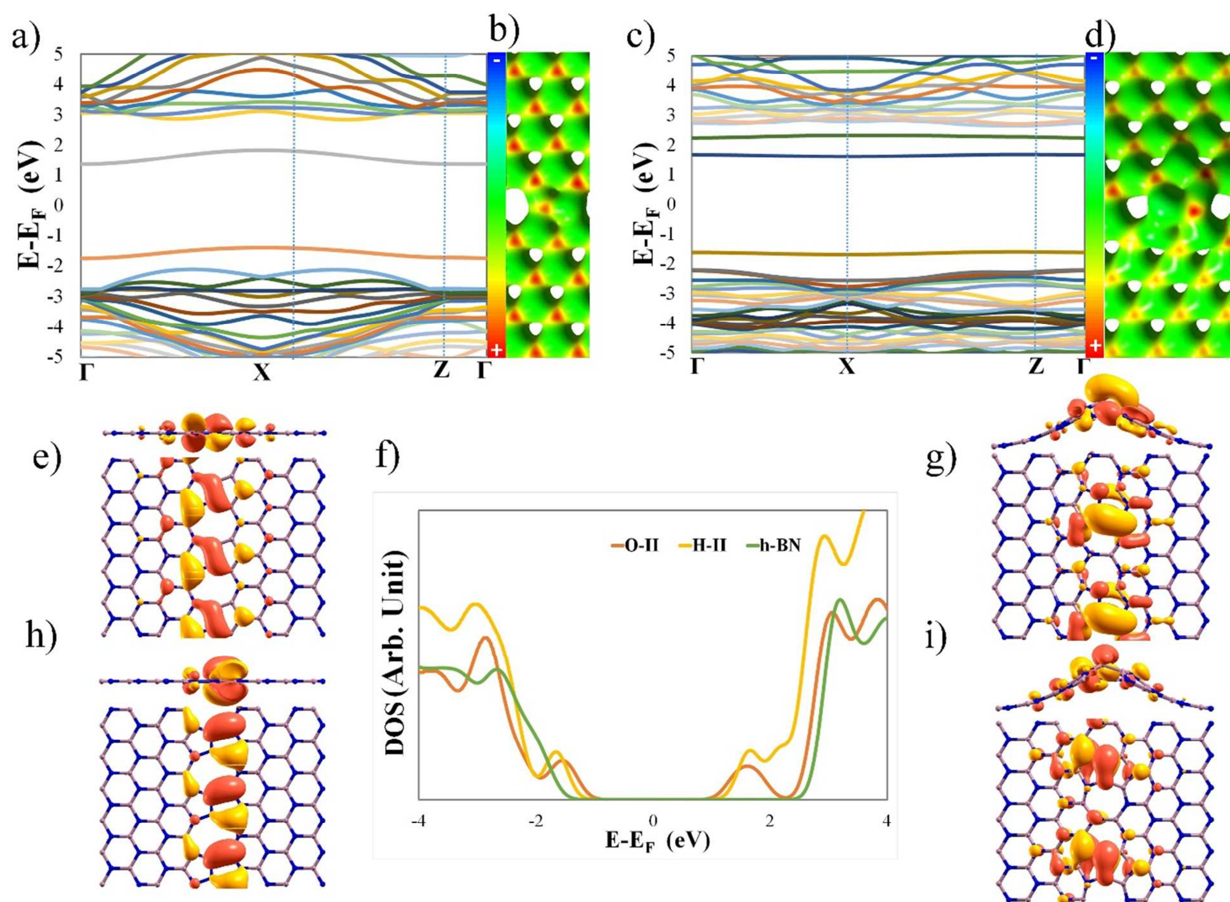

Physical Chemistry Chemical Physics Accepted Manuscript

Physical Chemistry Chemical Physics Accepted Manuscript

Figure 7.

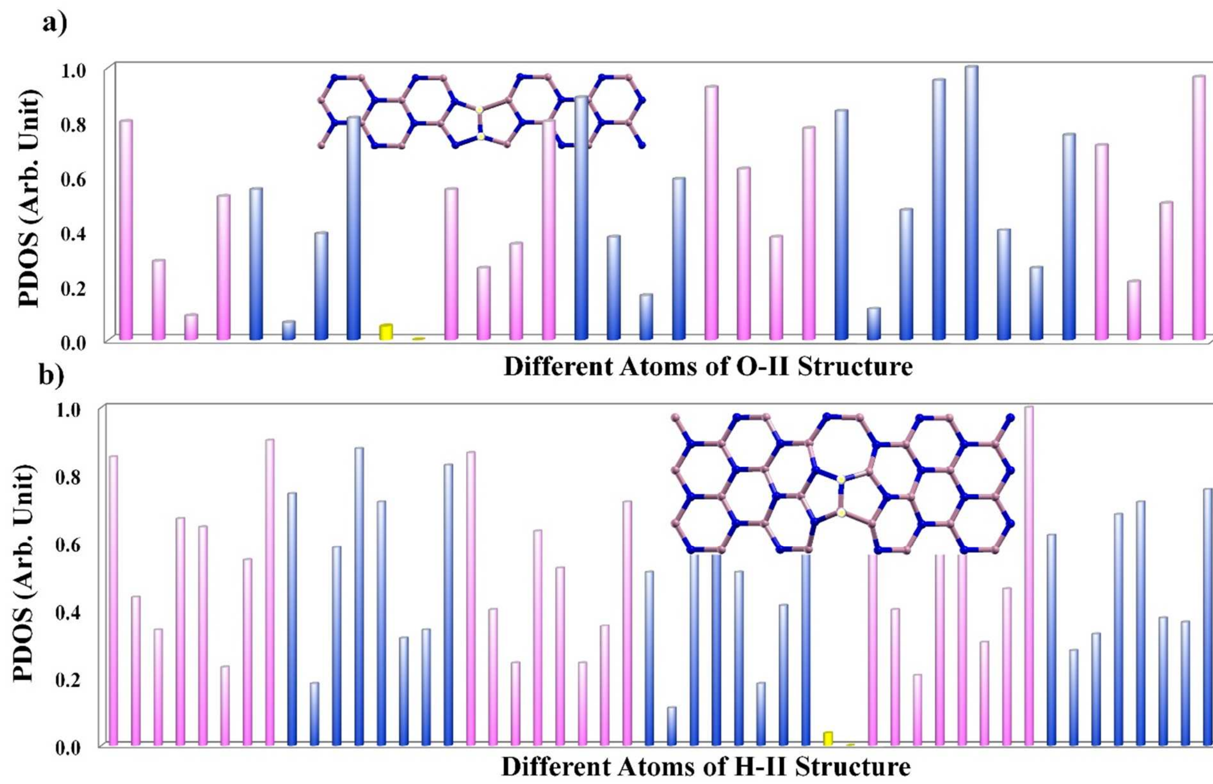

Figure 8.

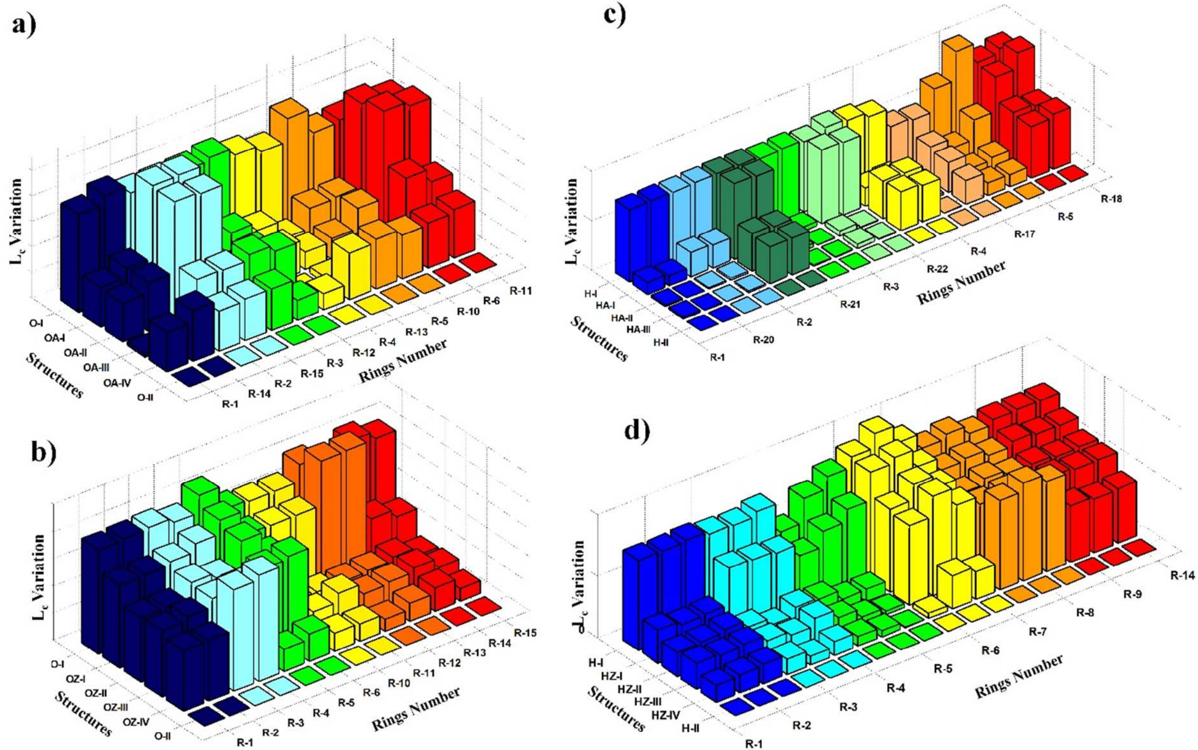

Physical Chemistry Chemical Physics Accepted Manuscript

Figure 9.

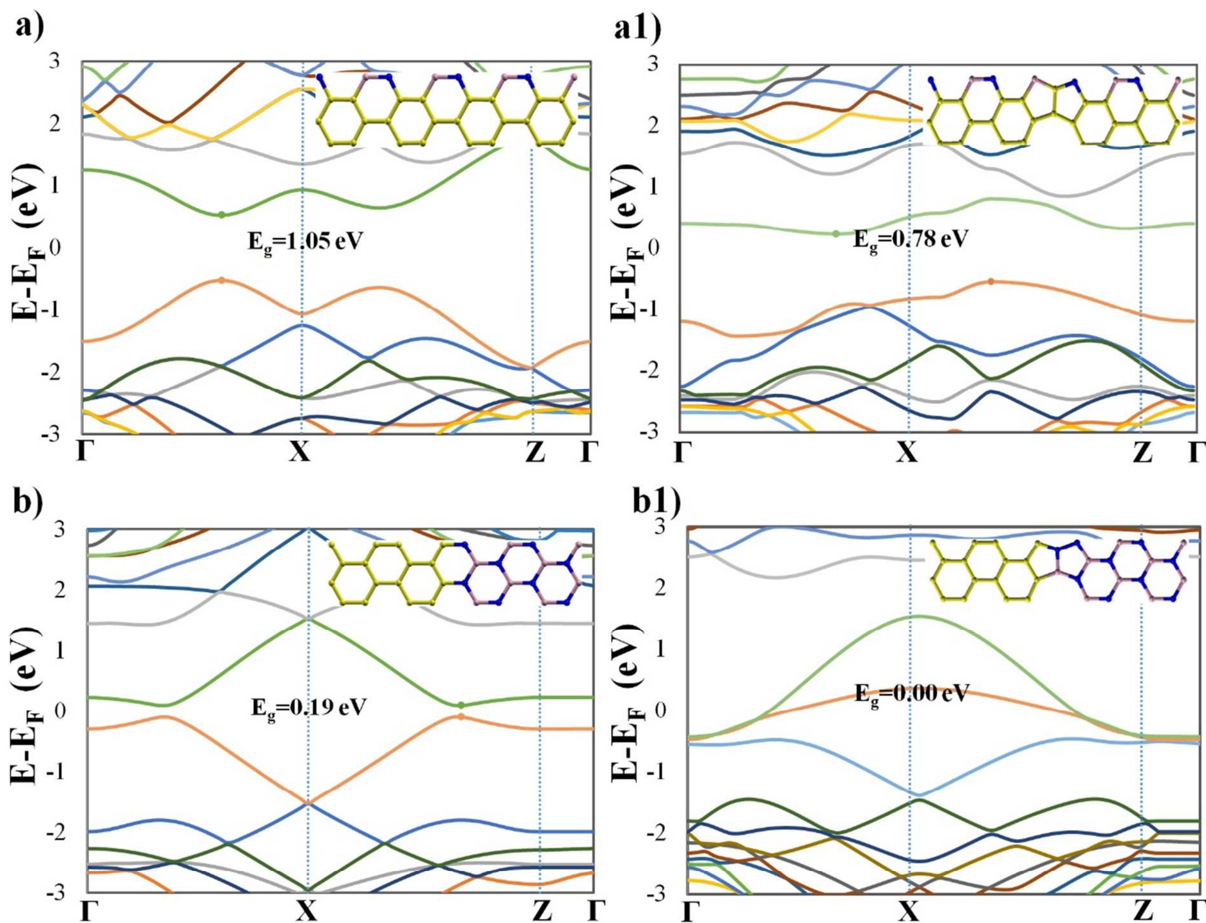

Physical Chemistry Chemical Physics Accepted Manuscript

Physical Chemistry Chemical Physics Accepted Manuscript

Figure 10.

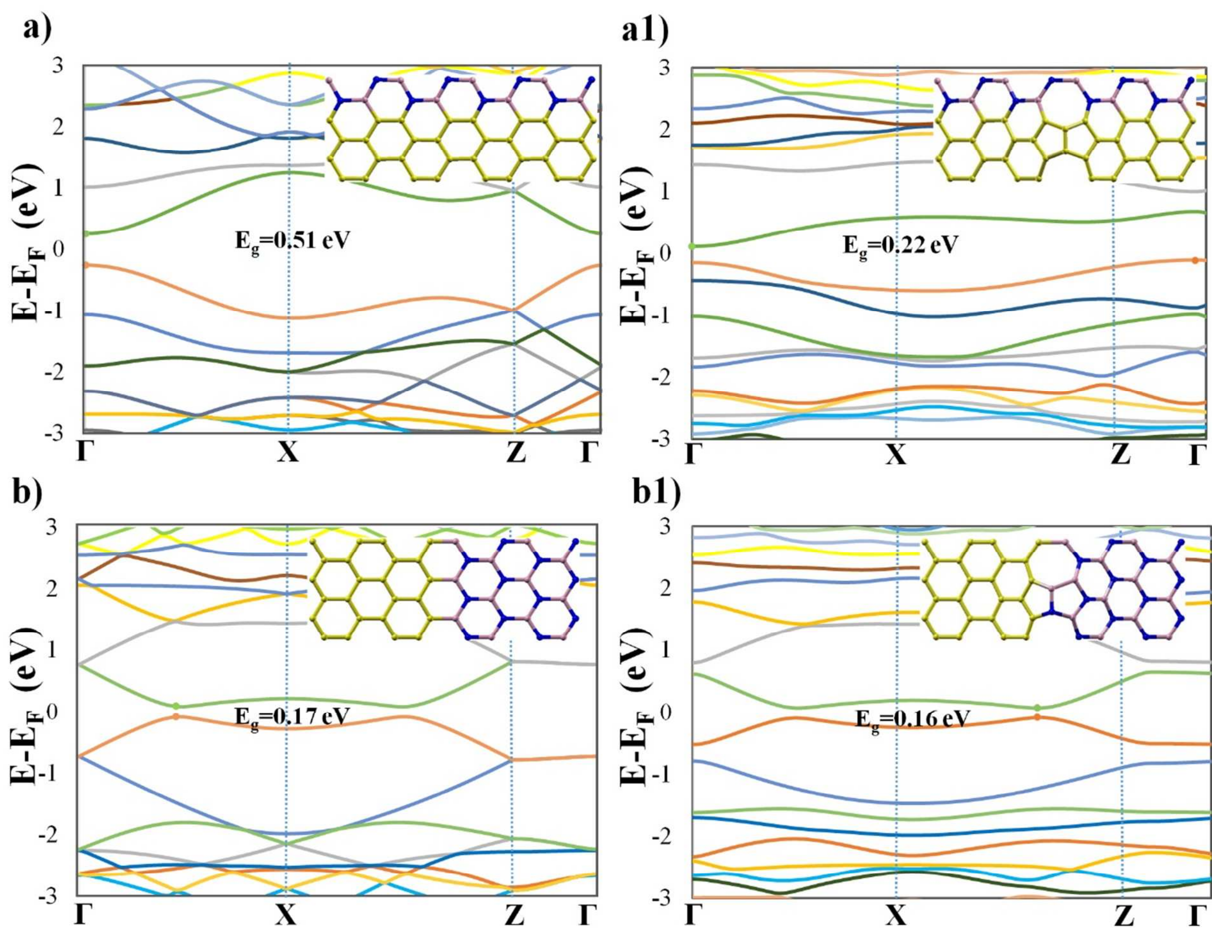

References

1 J. H. Davies, The Physics of Low-Dimensional Semiconductors. 6th ed., vol. 1, New York: Cambridge University Press, 2006.

2 A. C. Neto, F. Guinea, N. Peres, K. S. Novoselov and A. K. Geim, *Rev. Mod. Phys.*, 2009, **81**, 109.

3 A. K. Geim, *Science*, 2009, **324**, 1530.

4 D. A. Brownson, D. K. Kampouris and C. E. Banks*, J. Power. Sourc.*, 2011, **196**, 4873.

5 F. Schwierz, *Nature Nano.*, 2010, **5**, 487.

6 P. Avouris, *Nano Lett.*, 2014, **10**, 4285.

7 A. Neto and K. Novoselov, *Rep. Prog. Phys.*, 2011, **74**, 82501.

8 D. R. Dreyer, R. S. Ruoff and C. W. Bielawski, *Angew. Chem. Int. Ed.*, 2010, **49**, 9336.

9 M. Dvorak, W. Oswald and Z. Wu, *Sci. Rep.*, 2013, **3**, 1.

10 A. Botello-Mendez, X. Declerck, M. Terrones, H. Terrones and J.-C. Charlier, *Nanoscale*, 2011, **3**, 2868.

11 M. Ijas, M. Ervasti, A. Uppstu, P. Liljeroth, J. van der Lit, I. Swart and A. Harju, *Phys. Rev. B*, 2013, **88**, 075429.

12 L. Kou, C. Tang, T. Frauenheim and C. Chen, *J. Phys. Chem. Lett*., 2013, **4**, 1328.

13 G. Giovannetti, P. A. Khomyakov, G. Brocks, P. J. Kelly and J. van den Brink, *Phys. Rev. B*, 2007, **76**, 073103

14 X. Wang, X. Li, L. Zhang, Y. Yoon, P. K. Weber, H. Wang, J. Guo and H. Dai, *Science*, 2009, **324**, 768.

15 S. Mukherjee and T. Kaloni, J. *Nanopart. Res*., 2012, **14**, 1.

16 X. Wei, M.-S. Wang, Y. Bando and D. Golberg, *ACS Nano*, 2011, **5**, 2916.

17 W. Brito, R. Kagimura and R. Miwa, *Phys. Rev. B,* 2012, **85**, 035404.

18 G. Bepete, D. A. Voiry, M. Chhowalla, Z. Chiguvare and N. J. Coville, *Nanoscale*, 2013, **5**, 6552.

19 L. Panchakarla, K. Subrahmanyam, S. Saha, A. Govindaraj, H. Krishnamurthy, U. Waghmare and C. Rao, *Adv. Mater*., 2009, **21**, 4726.

20 S.-M. Choi, S.-H. Jhi and Y.-W. Son, *Phys. Rev. B*, 2010, **81**, 081407.

21 V. M. Pereira and A. C. Neto, *Phys. Rev. Lett*., 2009, **103**, 046801.

Physical Chemistry Chemical Physics Accepted Manuscript

22 R. T. Paine and C. K. Narula, *Chem. Rev*., 2014, **90**, 73.

23 Y. Lin and J. W. Connell, *Nanoscale,* 2012, **4**, 6908.

24 Q. Tang and Z. Zhou, Prog. *Mater. Sci*., 2013, **58**, 1244.

25 A. Nagashima, Y. Gamou, M. Terai, M. Wakabayashi and C. Oshima, *Phys. Rev. B*, 1996, **54**, 13491.

26 P. Srivastava, M. Deshpande and P. Sen, *Phys. Chem. Chem. Phys*., 2011, **13**, 21593.

27 J. M. Pruneda, Phys. Rev. B, 2010, 81, 161409.

28 J. Zhu, S. Bhandary, B. Sanyal and H. Ottosson, *J. Phys. Chem. C*, 2014, **115**, 10264.

29 L. Ci, L. Song, C. Jin, D. Jariwala, D. Wu, Y. Li, A. Srivastava, Z. Wang, K. Storr and L. Balicas, *Nat. Mater.,* 2010, **9**, 430.

30 N. Kumar, K. Moses, K. Pramoda, S. N. Shirodkar, A. K. Mishra, U. V. Waghmare, A. Sundaresan and C. N. R. Rao, *J. Matter. Chem. A*, 2013, **1**, 5806.

31 M. O. Watanabe, S. Itoh, T. Sasaki and K. Mizushima, *Phys. Rev. Lett.,* 1996, **77**, 187.

32 F. Banhart, J. Kotakoski and A. V. Krasheninnikov, *ACS nano*, 2010, **5**, 26.

33 J. C. Meyer, C. Kisielowski, R. Erni, M. D. Rossell, M. Crommie and A. Zettl, *Nano Lett.,* 2008, **8**, 3582.

34 A. Hashimoto, K. Suenaga, A. Gloter, K. Urita and S. Iijima, *Nature,* 2004, **430**, 870.

35 J. Song, H. Liu, H. Jiang, Q.-f. Sun and X. C. Xie, *Phys. Rev. B*, 2012, **86**, 085437.

36 H. Terrones, R. Lv, M. Terrones and M. S. Dresselhaus, *Rep. Prog. Phys.,* 2012, **75**, 062501.

37 M. T. Lusk, D. T. Wu and L. D. Carr, *Phys. Rev. B*, 2010, **81**, 155444.

38 A. AlZahrani and G. Srivastava, *Appl. Sur. Sci.,* 2010, **256**, 5783.

39 P. Rani and V. Jindal, *AIP Conf. Proc*., 2013, **1512**, 262.

40 P. Rani and V. Jindal, *Rsc Adv*., 2013, **3**, 802.

41 G. Lu, K. Yu, Z. Wen and J. Chen, *Nanoscale*, 2013, **5**, 1353.

42 H. Terrones and A. L. Mackay, *Carbon*, 1992, **30**, 1251.

43 O. V. Yazyev, *Rep. Prog. Phys*, 2010, **73**, 056501.

44 L. Kou, C. Tang, W. Guo and C. Chen, *ACS Nano*, 2014, **5**, 1012.

45 J. Lahiri, Y. Lin, P. Bozkurt, I. I. Oleynik and M. Batzill, *Nature Nanotechnol*., 2010, **5**, 326.

46 D. A. Bahamon, A. L. Pereira and P. A. Schulz, *Phys. Rev. B*, 2011, **83**, 155436.

47 S. Okada, K. Nakada and T. Kawai, *J. Phys.: Condens. Matter*, 2007, **19**, 365231.

Physical Chemistry Chemical Physics Accepted Manuscript

48 S. Okada, K. Nakada, K. Kuwabara, K. Daigoku and T. Kawai, *Phys. Rev. B*, 2006, **74**, 121412.

49 S. S. Yu, W. T. Zheng and Q. Jiang, Nanotechnol., *IEEE Trans*., 2010, **9**, 243.

50 Y. Li, R.-Q. Zhang, Z. Lin and M. A. Van Hove, *Appl. Phys. Lett.,* 2012, **101**, 253105.

51 C.-K. Chang, S. Kataria, C.-C. Kuo, A. Ganguly, B.-Y. Wang, J.-Y. Hwang, K.-J. Huang, W.-H. Yang, S.-B. Wang, C.-H. Chuang, M. Chen, C.-I. Huang, W.-F. Pong, K.-J. Song, S.-J. Chang, J.-H. Guo, Y. Tai, M. Tsujimoto, S. Isoda, C.-W. Chen, L.-C. Chen and K.-H. Chen, *ACS Nano*, 2014, **7**, 1333.

52 J. M. Pruneda, *Phys. Rev. B*, 2012, **85**, 045422.

53 L. P. Biro and P. Lambin, *New J. Phys*., 2013, **15**, 035024.

54 J. Kotakoski, A. V. Krasheninnikov, U. Kaiser and J. C. Meyer, *Phys. Rev. Lett*., 2011, **106**, 105505.

55 M. T. Lusk and L. D. Carr, *Phys. Rev. Lett.,* 2008, **100**, 175503.

56 P. Y. Huang, C. S. Ruiz-Vargas, A. M. van der Zande, W. S. Whitney, M. P. Levendorf, J. W. Kevek, S. Garg, J. S. Alden, C. J. Hustedt and Y. Zhu, *Nature*, 2011, **469**, 389.

57 O. V. Yazyev and S. G. Louie, *Phys. Rev. B*, 2010, **81**, 195420.

58 X. Li, X. Wu, X. C. Zeng and J. Yang, *ACS Nano*, 2014, **6**, 4104.

59 S. S. Alexandre, A. D. Lucio, A. H. Neto and R. W. Nunes, *Nano Lett.,* 2014, **12**, 5097.

60 O. V. Yazyev and S. G. Louie, *Phys. Rev. B*, 2010, **81**, 195420.

61 Y. Liu and B. I. Yakobson, *Nano Lett.,* 2014, **10**, 2178.

62 M. Deza, P. W. Fowler, M. Shtogrin and K. Vietze, *J. Chem. Inf. Comput. Sci*., 2014, **40**, 1325.

63 J. da Silva-Araujo, H. Chacham and R. W. Nunes, *Phys. Rev. B*, 2010, **81**, 193405.

64 N. Al-Aqtash, K. M. Al-Tarawneh, T. Tawalbeh and I. Vasiliev, *J. Appl. Phys*., 2012, **112**, 034304.

65 H. Zeng, C. Zhi, Z. Zhang, X. Wei, X. Wang, W. Guo, Y. Bando and D. Golberg, *Nano Lett.,* 2014, **10**, 5049.

66 K. H. Lee, H.-J. Shin, J. Lee, I.-y. Lee, G.-H. Kim, J.-Y. Choi and S.-W. Kim, *Nano Lett.,* 2014, **12**, 714.

67 W.-Q. Han, H.-G. Yu and Z. Liu, *Appl. Phys. Lett.,* 2011, **98**, 203112.

Physical Chemistry Chemical Physics Accepted Manuscript

68 A. J. Du, S. C. Smith and G. Q. Lu, *Chem. Phys. Lett.*, 2007, **447**, 181.

69 S. Tang and S. Zhang, *J. Phys. Chem. C*, 2014, **117**, 17309.

70 Y. Li, R.-Q. Zhang, Z. Lin and M. A. Van Hove, *Nanoscale,* 2012, **4**, 2580.

71 S. Okada, T. Kawai and K. Nakada, *J. Phys. Soc. Jpn*., 2011, **80**, 3709.

72 P. Giannozzi, S. Baroni, N. Bonini, M. Calandra, R. Car, C. Cavazzoni, D. Ceresoli, G. L. Chiarotti, M. Cococcioni and I. Dabo, *J. Phys.: Condens. Matter*, 2009, **21**, 395502.

73 J. P. Perdew, K. Burke and M. Ernzerhof, *Phys. Rev. Lett*., 1996, **77**, 3865.

74 W. E. Pickett, *Comput. Phys. Rep*., 1989, **9**, 115.

75 D. Vanderbilt, *Phys. Rev. B*, 1990, **41**, 7892.

76 H. J. Monkhorst and J. D. Pack, *Phys. Rev. B*, 1976, **13**, 5188.

77 P. P. Shinde and V. Kumar, *Phys. Rev. B,* 2011, **84**, 125401.

78 C. Jin, F. Lin, K. Suenaga and S. Iijima, *Phys. Rev. Lett*., 2009, **102**, 195505.

79 F. W. Averill, J. R. Morris and V. R. Cooper, *Phys. Rev. B*, 2009, **80**, 195411.

80 K. Watanabe, T. Taniguchi and H. Kanda, *Nat. Mater.*, 2004, **3**, 404.

81 X. Qin, Q. Meng, Y. Feng and Y. Gao, *Surf Sci*., 2012, **607**, 153.

82 Y. Xie, H. Yu, H. Zhang and H. Fu, *Phys. Chem. Chem. Phys*., 2012, **14**, 4391.

83 L. C. Gomes, S. S. Alexandre, H. Chacham and R. W. Nunes, *J. Phys. Chem. C*, 2013, **117**, 11770

Physical Chemistry Chemical Physics Accepted Manuscript